Atomistic Thermodynamics and Kinetics of Dicalcium Silicate Dissolution

2 Yong Tao^{1,2}, Siavash Zare¹, Fazhou Wang^{2,*}, Mohammad Javad Abdolhosseini Qomi^{1,*}

¹Department of Civil and Environmental Engineering, University of California, Irvine, California 92697,

United States

²State Key Laboratory of Silicate Materials for Architectures, Wuhan University of Technology. Wuhan, Hubei 430070, China

Abstract: Low-temperature cement manufacturing has garnered academic and industrial attention for its low environmental footprints. However, the sluggish hydration kinetics of the resultant cement affects their early-age strength development. This motivates fundamental studies to unravel the mechanistic picture of the dissolution process and discover science-informed pathways to accelerate hydration. Standard atomistic simulations seldomly exceed a microsecond making them impractical to study slow dissolution processes. Here, using rare event sampling techniques, we provide the mechanistic picture of Ca²⁺ ion dissolution from a kink site on the dicalcium silicate surface. The Ca²⁺ ion dissolution is comprised of two sequential stages: breaking restraints from the kink sites to form a ledge adatom and detaching from the ledge/terrace adatom sites into the solution. The first and second stages feature free energy barriers of ~63 kJ/mol and ~29 kJ/mol respectively, making the first stage the rate-limiting step of the entire Ca²⁺ dissolution kinetics. Using the reactive flux method, the rate and equilibrium constants for each reaction step are calculated, which yield the Ca²⁺ ion activity of ~1.03×10⁻⁵. The diffusion calculations indicate that the surface effects lower the self-diffusion coefficient of Ca²⁺ ions at the solid-

- 22 Keywords: Dicalcium Silicate; Dissolution; Thermodynamics; Kinetics; Atomistic Simulations; Rare
- 23 Event Sampling.

water interface.

1

3

4

5

6 7

8

9

10

11

12

13 14

15

16

17

18

19 20

21

24

1. Introduction

- Belite, an impure form of dicalcium silicate (Ca₂SiO₄: C₂S), is the second most abundant component in
- the ordinary Portland cement (OPC) clinker[1]. With a lower calcium-to-silicon ratio compared to alite,
- 27 impure tricalcium silicate (Ca₃SiO₅: C₃S), belite's production requires ~30% less limestone and
- 28 proportionally releases less carbon dioxide during the calcination process. Additionally, the formation
- enthalpy of belite (~1350 kJ/kg) is much lower than that of alite (~1810 kJ/kg)[2]. This formation
- 30 enthalpy difference leads to a lower clinkerization temperature of ~1250 °C for the "low-energy" belite
- 31 cement compared with ~1450 °C for the commercial OPC clinker[3] and as a result belite manufacturing
- 32 has a lower energy footprint. These attributes have made belite cement a promising solution for the

development of sustainable cement formulations[3]. Despite the interest in producing low-temperature cements, their low reactivity and poor early-age strength development[4] are major drawbacks that hold their adoption back by concrete construction practitioners and regulating agencies. These technical impediments motivate basic studies to understand the origins of belite's slow reaction kinetics in the hope to leverage this fundamental understanding to devise cost-effective science-informed approaches to activate belite's hydration[5].

 While the cement hydration spans from seconds to centuries[6], experimentalists pay special attention to the acceleration period[7] that embodies the macroscopic characteristics of clinker hydration. At the very beginning of cement hydration, hydraulic clinker minerals rapidly dissolve without significant interference from solution environments, whose kinetics is representative of the intrinsic reactivity of cement clinker[7, 8]. The dissolution process is a rate-limiting step at this stage that involves the abstraction of ions from mineral surfaces to the solution. New experimental techniques have notably paved the path for improved understanding of the early-age dissolution processes. For instance, Thomas et al.[9, 10] proposed a calorimetry-based approach to measure the instantaneous hydration activation energy by rapidly changing the temperature of a single hydrating sample. Nicoleau et al.[11] designed a unique experimental set-up with the inductive coupled plasma-optical emission spectrometer to measure the dissolution kinetics and solubility products of C₂S and C₃S in the absence of calcium silicate hydrates (C-S-H). Brand et al. [8, 12, 13] used the in situ digital holographic microscopy to characterize the surface dissolution flux of tricalcium aluminate (Ca₃Al₂O₆: C₃A) and C₂S. Myers et al.[14] combined X-ray absorption spectroscopy and zeta potential measurements to develop a qualitative C₃A hydration model that highlights the role of Ca-S ion-pair adsorption on Al-rich Ca-leached surfaces in regulating the earlyage dissolution kinetics in OPC systems. Additionally, the high-speed frequency modulation atomic force microscopy has provided nanoscale information regarding step morphology, etch pit generation frequencies, and step retreat rate in geochemical systems[15, 16], which can also be translated to cement chemistry studies.

Theoretical models and simulation techniques provide toolsets to correctly interpret dissolution experiments and contribute to developing quantitative frameworks to estimate hydration kinetics in complex cement systems[17]. Adopting a theoretical geochemistry approach[18], Juilland *et al.*[19] proposed a model that combines the dissolution process from crystallographic defects and solution saturation to describe the induction period. This model suggests that the initially fast clinker dissolution is due to the massive etch pit formation processes on clinker surfaces. It also proposes that when the solution's undersaturation level becomes smaller than the critical undersaturation, a slow surficial "step retreat" mechanism dominates the dissolution process and accounts for the start of the induction period.

More involved three-dimensional microstructure simulations based on the probabilistic cellular automaton algorithms, *e.g.*, Bullard's HydratiCA model [20], provide a mechanistic picture of cement hydration at the microscale and the competition between dissolution and surface coverage by hydration products. To provide a more fundamental insight, Martin *et al.*[21] have recently developed a kinetic Monte Carlo (KMC) model to simulate the dissolution process in cement minerals. The KMC approach predicts the dissolving surface's topographical evolution, the dissolution rate, and associated thermodynamic energy barriers[22, 23]. Regardless of their complexity, the abovementioned models require fundamental thermodynamic and kinetic inputs that are either calibrated via experiments or computed from molecular simulations.

Molecular simulations can in principle deliver the fundamental physicochemical properties of clinker minerals, *e.g.*, crystal structure[24], doping effects[25], surface stability[26], surface adsorption and hydroxylation[27], and reactivity[28]. However, thus far, they have failed to provide a mechanistic picture of the dissolution process and the corresponding thermodynamics and kinetic properties. This failure is intimately related to the probability of observing the dissolution process within the limited reach of atomistic simulations. Indeed, if molecular dynamics (MD) simulation time is increased to the macroscopic time scales, thermodynamic fluctuations will eventually trigger the dissolution in MD simulations. However, the classical MD seldomly exceeds a microsecond due to the prohibitive computational cost. To put this in the statistical mechanics perspective, the dissolution is a low-probability "rare event" [29] that cannot be ergodically sampled within the classical MD framework. To address this shortcoming, researchers have developed computational schemes to explore the so-called rare events, *e.g.*, metadynamics[30], umbrella sampling[31, 32], adaptive biasing force[33], and free energy perturbation [34]. Essentially, these advanced simulation methods explore the free energy landscape by adding a biasing function, *i.e.*, a penalty force or potential, across predefined reaction coordinates. We can employ these advanced toolsets to study the rare dissolution events at the nanoscale.

In this paper, we leverage a newly-developed classical force field, ClinkerFF, to study the abstraction of a calcium ion from a kink site of the β -C₂S surface. To this end, we combine metadynamics and umbrella sampling methods to calculate the dissolution free energy landscape, demonstrating the nanoscale mechanistic picture of elementary steps involved in the dissolution process and their corresponding energy barriers. Based on the calculated free energy profile, we further use the transition state theory and the reactive flux method to compute dissolution's kinetic constants (*e.g.*, transmission coefficients, dissolution rate constants, equilibrium constants, and ion activity). Finally, we perform diffusion calculations to demonstrate the surface effects on the self-diffusion of Ca²⁺ ions in the solution.

2. Methodology

2.1 Development of ClinkerFF Potential: The predictive power of atomistic simulations is contingent on the transferability of the classical force field that describes interatomic and intermolecular forces and energies. Numerous force fields have so far been developed for cementitious materials; we refer interested readers to the comprehensive comparative literature review by Mishra et al.[35]. For the accurate description of interatomic forces during the dissolution process, we require a force field that can adequately describe the variation of point charges on dissolving ions. Such description would, in principle, require a variable charge and polarizable force field. The variable charge schemes are implemented for instance in ReaxFF, which is extended by Manzano et al.[36] to study calcium silicates. As will be discussed in section 2.3, dissolution simulations require rare event sampling techniques that are computationally prohibitive and perhaps inaccurate with ReaxFF-type force fields. Accordingly, we choose to work with classical non-polarizable force fields with fixed charges, such as ClayFF[37] that is widely used for clays and cementitious materials. However, the partial charge of structural calcium in ClayFF is +1.36 compared to the charge of +2 for dissolved calcium cations in the solution to investigate calcium dissolution[38]. Another drawback of adopting ClayFF for Ca²⁺ dissolution simulations is that it overestimates the attractive force between the surface and the adsorbed water molecules and hydroxyl groups. This discrepancy directly alters the structure of the interfacial adsorbed water layers, reduces the adsorbate-surface distance, and increases the magnitude of the associated adsorption energies [39]. These drawbacks render ClayFF inapplicable to studies of Ca²⁺ ion dissolution from silicate surfaces.

99 100

101

102103

104

105106

107

108

109

110

111

112

113114

115

116

117

118

119120

121

122

123124

125

126127

128129

130

131

To study interfacial phenomena and dissolution processes on cement mineral surfaces, we have developed a new force field called ClinkerFF. The development of ClinkerFF is inspired by magnesium silicates force fields developed by Kerisit et al. [38] in the computational geochemistry community. The charge of calcium is fixed to +2, while the silicon charge is kept the same as that in ClayFF. The charges of oxygen atoms are modified accordingly to ensure electric charge neutrality. The partial charges of species are provided in **Supplementary Table 1**. In ClinkerFF, intramolecular bond and angle coefficients in water molecules and hydroxyl groups are fixed to the original ClayFF values, **Supplementary Table 2**. Since ClinkerFF is designed with the dissolution of cations in mind, it should faithfully reproduce the structural attributes, hydration energy, water exchange rate, and transport properties of dissolved Ca²⁺ ions as a limiting case. While Kerisit and Parker [40] developed a polarizable force field for Ca²⁺-H₂O systems, Raiteri *et al.* [41] developed a non-polarizable force field using Lennard-Jones potential to successfully calibrate properties of alkaline-earth cations in the solution. It is noteworthy that Raiteri *et al.*'s formulation [41] can accurately simulate the thermodynamic properties (Gibbs free energy, enthalpy, and entropy change), geometric structure of Ca²⁺-H₂O complex (bond distances and coordination number), water exchange rate to the first hydration shell, and its self-diffusion constant in bulk water. See

Supplementary Table 3 for the comparison of Raiteri et al.'s Lennard-Jones formulation with the available experimental and simulation data[40]. For the sake of simplicity and congruency with ClayFF formulation, we adopt Raiteri et al.'s [40] Lennard-Jones parameter set and avoid a more involved polarizable force fields to describe the interactions between Ca²⁺ ions and oxygen atoms of water molecules.

The rest of Lennard-Jones parameters in ClayFF are accordingly reparametrized to reproduce the lattice constants, elastic properties, structural attributes, adsorption energy and adsorbate structure on mineral surfaces. Supplementary Table 4 compares the calculated and measured lattice constants, bulk, shear, and Young's moduli, Possion's ratio, bond distance and bond angle in silicate monomers between ClinkerFF, ClayFF, available density functional theory calculations (DFT) [42, 43], and experimental data [44-46]. Supplementary Table 5 presents the associative water and dissociative hydroxyl group adsorption energy and structures for geometries presented in Supplementary Figure 1. ClinkerFF's adsorption data are compared against those of ClayFF and DFT calculations using Perdew-Burke-Ernzerhof [47] pseudopotentials with the projector augmented plane wave (PAW) [48] and dispersion correction using the method of Grimme [49] at DFT-D3 level of theory, for details consult Supplementary Section 1.2. The force field parameterization is performed using the full BFGS method (calculating the full numerical Hessian matrix) implemented in GULP [50] and the optimization is initialized from multiple starting points on a grid to escape from regions with gentle gradients. ClinkerFF's Lennard-Jones parameters are provided in Supplementary Table 6.

2.2 Construction of the Kink Surface Structures: β -C₂S crystal, the main phase of belite, is chosen here to simulate belite dissolution. The crystal structure of β -C₂S is adopted from the work of Jost *et al.*[45]. We note that hydration might potentially change the stability of β -C₂S surfaces. Here, due to the absence of experimental data, we limit our attention to the available theoretical data on β -C₂S surface stability. Previous DFT calculations have already shown that (1 0 0) surface is the most stable among seven low-index cleavages [26]. ClinkerFF surface energy calculations also confirm that (1 0 0) surface is the most stable surface of β -C₂S. For this reason, we choose the (1 0 0) surface in our dissolution studies. From the classical thermodynamics of surface formation and transformation perspective[51, 52], various surface configurations form during the dissolution process, such as terrace, step (also known as ledge), and kink to only name a few. Experimental and theoretical studies show that the advancement of kink sites is the rate-limiting step of surface dissolution or growth[53, 54]. Therefore, this paper focuses on the dissolution processes from kink sites. Here, we construct the kink structure by deleting stoichiometric (charge neutral) units from the top and bottom layers of a flat (1 0 0) surface. Different kink configurations and surface terminations are thoroughly examined to ensure zero dipole components in all

directions to eliminate unrealistic charge-dipole interactions during the dissolution process. The surface size of the kink model has been tested to ensure the interactions of the kink sites and their periodic images are negligible (**Supplementary Figure 2-4**). The selected kink structure has a size of 49.7 Å × 44.1 Å × 68.3 Å with a water layer thickness of 40 Å as depicted in **Fig. 1**. The pristine β -C₂S has two calcium types that exhibit different chemical environments [55, 56]; a seven-coordinated and an eight-coordinated calcium atoms that are respectively denoted by Ca1 and Ca2 in **Fig. 1**. We implement the metadynamics simulations with these two types of calcium atoms as kink sites respectively to determine the rate-limiting dissolution step (**Fig. 1**).

Surface hydroxylation is also important when studying the mechanistic picture of dissolution at the nanoscale. High-resolution X-ray reflectivity[57], thermogravimetric analysis, and inelastic neutron scattering[58] experiments indicate that the (0 1 0) surface of dimagnesium silicate (forsterite) is hydroxylated in ambient conditions. While we acknowledge that these experiments are performed on magnesium-rich systems, we believe they can act as a proxy to understand interfacial phenomena in other metal silicate systems such as C₂S. Utilizing inductive coupled plasma-optical emission spectroscopy technique for C₃S and C₂S dissolution, Nicoleau *et al.*[11] emphasize that superficial hydroxylation is of prime significance in the dissolution process. Both atomistic simulations and DFT calculations confirm the hydroxylation of forsterite[59], alite[27], and belite[60] surfaces.

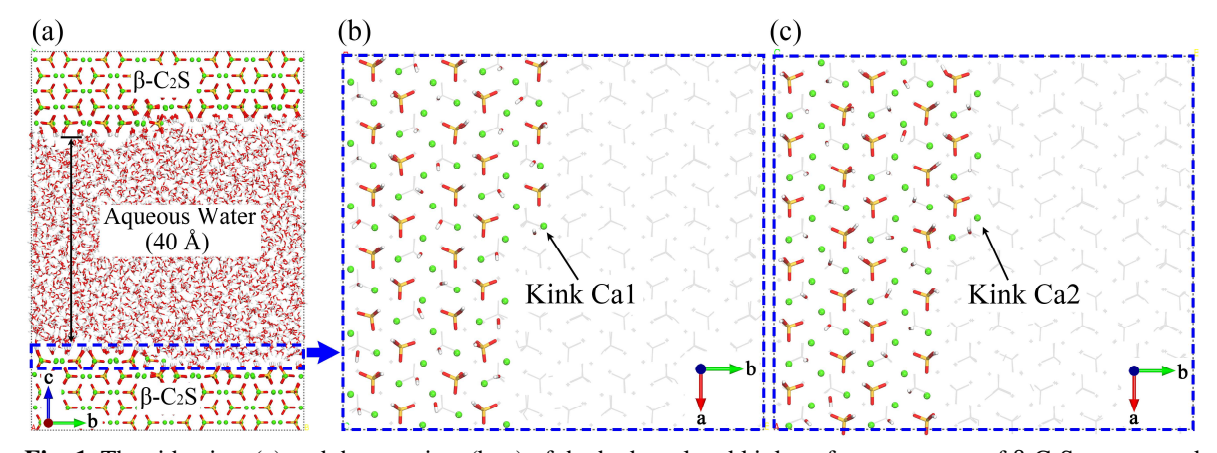


Fig. 1. The side view (a) and the top view (b, c) of the hydroxylated kink surface structures of β -C₂S constructed for dissolution calculations. The green spheres represent calcium atoms, orange-red sticks are silicate monomers, and water molecules (H₂O, OH⁻) are shown in white-red sticks. Some atoms in the top view are hidden for the sake of clarity. The two types of calcium (Ca1 and Ca2) on the β-C₂S (1 0 0) surface are investigated as the kink atoms respectively in this study.

To hydroxylate the kink surface structure presented in **Fig. 1**, we perform ReaxFF[36] calculations on the clean surfaces at elevated temperatures to artificially accelerate the rate of chemical reactions to reduce the computational cost. For ReaxFF simulations, we use LAMMPS[61] package and set the MD time step

to 0.1 fs. Employing the Nose-Hoover thermostat and canonical (NVT) ensemble, the slab is heated from 300 K to 1000 K within 500 ps and equilibrated at 1000 K for 2 ns. Subsequently, the system is annealed to room temperature within 500 ps and equilibrated for 1 ns to obtain final hydroxylated surfaces. The top and bottom surfaces are fully hydroxylated (2.76 OH/nm²) at the end of the ReaxFF simulation. More information about the surface hydroxylation results is presented in Supplementary Materials (**Supplementary Figure 5, 6**). After dissociative adsorption simulations, we saturate the slit pore (vacuum space) with SPC water at the density of 1 g/cm³. The simulation box is subsequently relaxed in an isothermal isobaric ensemble using a Nose-Hoover thermostat and barostat to release the residual stresses.

2.3 Rare Event Sampling and Kinetics Calculations: For the rare event sampling simulations, we use a combination of metadynamics [62] and umbrella sampling [63] methods. With minor adjustments, our approach is similar to the work of Stack *et al.* [54] who studied the barium dissolution from a step site on barite surface. For metadynamics calculations, bias Gaussian functions are continuously added to fill up the free energy basins. At the end of the simulation, the sum of the added Gaussians equals the negative of the free energy. The advantage of metadynamics is that it does not require an *a priori* knowledge of accurate reaction pathways. Otherwise stated, the system automatically explores the free energy landscape and finds important intermediate states within the free energy basin. However, the drawback of metadynamics is that the free energy barriers are sensitive to Gaussian parameters (height, width, bias factor, and frequency of addition), see Supplementary Materials (**Supplementary Figure 7**). Basically, when the Gaussian size (height and width) and addition frequency become smaller and smaller, the free energy profiles gradually converge. Indeed, by carefully choosing the Gaussian parameters, the metadynamics results are shown to converge (**Supplementary Figure 8**). However, while the free energy barriers are sensitive to Gaussian parameters, the local minima are almost the same, because the system usually stays at the local minima for a relatively long time, resulting in sufficient sampling.

In contrast to metadynamics, umbrella sampling can precisely calculate the free energy barriers along a prespecified reasonable reaction path. However, defining a reasonable reaction path for a complex reaction mechanism is far from trivial[63]. Therefore, to take advantage of these two methods, we initially perform an exploratory metadynamics simulation only to explore and estimate the free energy landscape and intermediate states. Then, we use the nudged elastic band (NEB) method [64] to search for an approximate minimum free energy pathway (MFEP) between adjacent intermediate states. Finally, the free energy barriers along each MFEP are refined with umbrella sampling that we merge together to resolve the Ca²⁺ dissolution free energy profile.

For both metadynamics and umbrella sampling, the selection of collective variable (CV) is pivotal to the accuracy of free energy calculations. The ion-kink separation distance $(r_{\text{ion-kink}})$ is a commonly used CV to investigate the ion dissolution from a mineral surface [65-67]. Joswiak et al. [65] studied the Na⁺ and Cl⁻ ion dissolution at kink sites on NaCl surfaces. They found that for Na+ ion dissolution, rion-kink outperformed alternative choices of the solute CV (i.e., coordination number, height above the surface, etc.) and even outperformed pairs of abovementioned solute CVs. For Cl⁻ ion dissolution, however, the $r_{\text{ion-kink}}$ alone was reported to be insufficient. This is because Na⁺ and Cl⁻ ions exhibit different water exchange rates in the solution. As summarized by previous studies [68, 69], for those ions that feature large water exchange rate constants (e.g., Na⁺, K⁺, Ca²⁺, Sr²⁺, etc.), the r_{ion-kink} alone is a good CV. However, the cation's coordination number with water must be considered as a CV for ions exhibiting small water exchange rates (e.g., Al³⁺, Fe³⁺, Mg²⁺, Ni²⁺, etc.). We also note that the water exchange rate of ions on the surface is lower than that in the solution[70], the decision to exclude water coordination number as an additional CV must be exercised with caution. Our preliminary metadynamics calculations considering the water coordination number as an additional CV indicate that the free energy landscape is not considerably changed by such addition, despite excessive computational cost. Therefore, for metadynamics simulations in this work, the three cartesian coordinates of Ca2+ ions are set as the collective variables to explore the three-dimensional free energy landscape of Ca²⁺ dissolution. For umbrella sampling simulations, the collective variable is the absolute distance between the dissolved Ca²⁺ and the initial kink site. The adoption of three cartesian coordinates introduces complications in sampling the free energy landscape. In particular, at relatively large Ca^{2+} -surface separation distance, r, the increase in entropy favors Ca²⁺ dissolution and exploration of energetically accessible states within the solution. Considering the Boltzmann entropy, such entropic interactions scale with $ln(r^3)$ and the resultant forces scale with r^{-1} . In the meantime, the dissolving Ca^{2+} ion is attracted back toward the surface via a screened coulombic interaction that scales with r^{-1} for small distances and scales with r for very large distances, where $\frac{d}{dt} \ll 1$ (d being the periodic cell size) and the surface can be viewed as a uniformly charged slab. In the former case, the electrostatic forces scale with r^{-2} and in the latter case, the cation experiences a constant attractive force. At intermediate distances, these entropic and coulombic interactions are in competition. In the intermediate regime, the coulombic interaction decay and the entropic forces stabilize the solution state, though this is dependent on the ion concentration in the solution. From the

computational perspective, however, calculations of the competitions between coulombic and entropic

forces are exceedingly expensive due to the need to adequately sample the configurational space that

scales with r^2 . With such subtleties in mind, we focus our free energy calculations within a 7 Å cut-off

218

219

220

221222

223224

225

226227

228

229230

231

232

233

234

235236

237

238

239

240

241

242

243

244

245246

247

248

249

250

radius beyond which strong surface Ca-O chemical bonds are absent and entropic contributions dominate free energy perturbations.

The metadynamics and umbrella sampling calculations were performed with LAMMPS [61] patched with the PLUMED [71] package. After extensive convergence testing, see Supplementary Materials (Supplementary Figure 7-9), the Gaussian potentials with a width of 0.1 Å and a height of 0.4 kJ/mol are added every 250 time steps. Choosing the well-tempered metadynamics [72] flavor, we set the bias factor to 10. The metadynamics simulations last for 60 ns and are terminated when Ca²⁺ ions are fully dissolved into the solution. For umbrella sampling simulations, the initial MFEP explored by NEB is divided into 135 windows with a width of 0.06 Å. In each window, the system is constrained by a spring (harmonic potential) with a stiffness constant of 350 kJ/mol/Å² and sampled for 2 ns to produce enough energy overlap statistics. All simulations are performed in the NVT ensemble at 300 K using Nose-

Hoover thermostat with a time step of 1 fs using ClinkerFF potential, see **section 2.1**.

Having MFEP at hand, the dissolution kinetic constants, *e.g.*, reaction rate and equilibrium constants, can be measured via statistical mechanics techniques. The rate constant (k) is the product of transition state theory rate constant (k^{TST}) and transmission coefficient (κ) [73]:

$$k = \kappa k^{\text{TST}} \tag{1}$$

We use the MFEP profiles to directly calculate k^{TST} as follows:

268
$$k^{TST} = \frac{e^{-A_{TS}/k_B T}}{\int_{-\infty}^{TS} e^{-A(q)/k_B T} dq} \sqrt{\frac{k_B T}{2\pi\mu}}$$
 (2)

where μ is the mass change during the reaction, set here to the mass of the dissolving calcium ion, k_B is the Boltzmann constant, and T represents temperature. A_{TS} designates the free energy difference between the reactant and transition states (TS). $\int_{-\infty}^{TS} e^{-A(q)/k_BT} dq$ is the integral of the free energy on the reaction path q from the reactant state $(-\infty)$ to the TS. The reactive flux method (RFM)[74] provides transmission coefficient κ in eq. (1). For RFM simulations, we first generate a representative set of configurations on TS (dividing surface) by running MD simulation in the NVT ensemble while fixing the TS structure (Ca²⁺ ion and connected oxygen atoms from silicate monomers). Subsequently, each configuration is initialized by assigning multiple Boltzmann distributed momenta and TS structures are released to find either the reactant or the product states. The convergence tests (Supplementary Figure 10) show that 2000 configurations with 5 trajectories per configuration are enough to accurately estimate κ . The forward and backward trajectories are monitored in the microcanonical ensemble (NVE) and the re-crossing ratio of

trajectories are continuously computed to provide a time-dependent transmission coefficient function, $\kappa(t)$. The limit of $\kappa(t)$ at infinite time yields κ as follows:

282
$$\kappa = \lim_{t \to \infty} \frac{\langle \dot{q}(0)h[q(t) - q(0)] \rangle_{q = q^{TS}}}{\langle \dot{q}(0)h[\dot{q}(0)] \rangle_{a = q^{TS}}}$$
 (3)

where $\dot{q}(t)$ is the time-dependent velocity of trajectories, q(t) is the time-dependent position of trajectories released from TS (q^{TS}) , h(q) is the Heaviside function, and <> operator denotes the statistical ensemble average. For practical purposes, the plateau value of the $\kappa(t)$ is usually taken as the estimate of κ .

2.4 Diffusion Calculations: To better understand the surface effects on the diffusion properties of Ca^{2+} ions in solution, we construct atomistic models of Ca^{2+} diffusion in the solution of a kink surface slab, a flat surface slab, and a water box, respectively (**Fig. 2**). All three models have the same solution volume (59 Å × 59 Å × 38 Å), while the slab of β -C₂S has a thickness of about 30 Å. Twelve Ca^{2+} ions and 24 OH⁻ ions are randomly scattered in the aqueous solution. It is worth noting that due to the low solubility of $Ca(OH)_2$, the simulated solution is checked to be oversaturated. Thus we in fact are calculating the Ca^{2+} ion diffusion properties in the saturated $Ca(OH)_2$ solution. In these simulations, the system is first equilibrated in the NVT ensemble for 1 ns and additionally for 100 ps in the NVE ensemble to eliminate the thermostat effect. The diffusion dynamics are subsequently monitored and sampled in the NVE ensemble for 10 ns recording Ca^{2+} ion diffusion trajectories every 5 ps. To calculate the Ca^{2+} ion's self-diffusion activation energy barrier, the diffusion coefficients are calculated at temperatures from 280 K to 360 K at 20 K increments. We use Einstein relation to compute the self-diffusion coefficient (*D*) on recorded MD trajectories:

$$300 D = \frac{1}{2N} \lim_{t \to \infty} \frac{MSD(t)}{t} (4)$$

where N is the dimensionality that is three for the bulk diffusion[75], the mean square displacement $(MSD(t) = \langle |r(\tau + t) - r(\tau)|^2 \rangle)$ designates the ensemble average of square atomic displacements. Since diffusion is an equilibrium (stationary) process, the proper averaging is performed considering the position of all Ca²⁺ ions, r, at different τ time lags along each MD trajectory to reduce noise and statistical error.

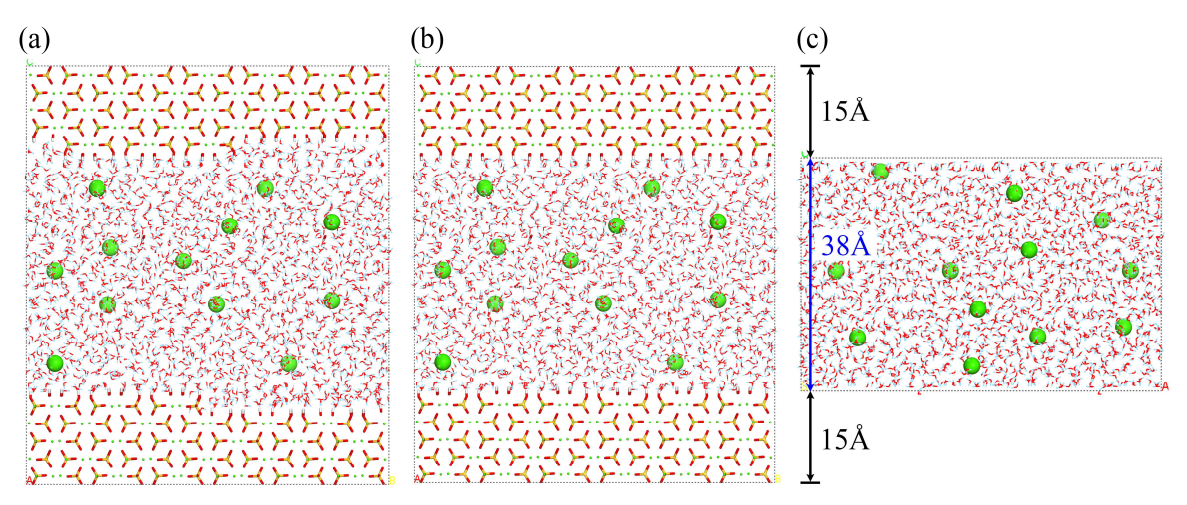


Fig. 2. Molecular models for the comparison of surface effects on the Ca²⁺ ion dissolution: diffusion in the solution of a kink surface slab (a), a flat surface slab (b), and a water box (c). The green spheres represent calcium atoms (calcium ions in solution are magnified), orange-red sticks are silicate monomers, and water molecules (H₂O, OH⁻) are shown in blue-red sticks. All the three models have the same volume of solution (59 Å \times 50 % \times 29 %)

3. Results and Discussions

306

307

308

309

310

311

312

313

314

315

316

317318

319

320

321

322

323

324

325

326

3.1 The Mechanistic Picture and Energetics of the Dissolution Process: Metadynamics simulations indicate that Ca1 features much lower dissolution free energy barriers than Ca2 (Supplementary Figure 4). Therefore, we focused on the dissolution of the Ca2 site as it is the rate-limiting step of the β-C₂S dissolution process. Fig. 3 shows the dissolution free energy profile calculated by refining metadynamics results via the umbrella sampling method. The schematics on the right side of Fig. 3 depict the coordination structure of the dissolving Ca²⁺ ion at local free energy minima and transition states along the dissolution pathway. The black and pink dashed lines respectively depict the chemical bonds (coordination) of the Ca²⁺ ion with the silicate monomers of the initial kink site and water molecules (H₂O and OH⁻), while the green dashed lines show the chemical bond formation of the Ca²⁺ ion as a ledge adatom. Generally, the entire Ca²⁺ ion dissolution process is composed of two stages: breaking restraints from the kink sites to form a ledge adatom and detaching from the ledge/terrace adatom sites into the solution. This process is similar to the dissolution of gibbsite from the step edge as investigated by Shen et al. [67]. For the first stage, the Ca²⁺ ion first shifts a small displacement from the initial kink site (state S1) to S2 by overcoming a slight free energy barrier of 11.9 kJ/mol. S2 is also a kink site for the Ca²⁺ ion that forms three chemical bonds with the silicate groups on the surface in contrast to the initial kink site (S1) that has four chemical bonds between the Ca²⁺ ion and silicate. Based on the free energy profile, S2 is the most stable state during the Ca²⁺ dissolution process. It is not surprising that S1, the initial kink site, is not the most stable state since Ca²⁺ at the initial kink site is highly uncoordinated compared with Ca²⁺ on the flat surface or in the bulk crystal. Similar observations have been reported in the previous study of barite dissolution by Stack *et al.* [54], where they found the inner-sphere adsorption is the most stable state of the barium ion during the dissolution.

The Ca²⁺ ion at S2 needs to over a high-energy state (TS2) to reach S3, known as the "inner-sphere adsorption" in the geochemistry community [54], which is bound only by one chemical bond on the kink site. Ca²⁺ at S3 behaves in higher flexibility with larger accessible regions compared to the initial kink site, causing a wide basin with several small humps in the free energy profile as shown in **Fig. 3**. As the inner-sphere adsorption (S3) breaks the last chemical bond with the kink site, the Ca²⁺ ion forms a new chemical bond with the silicate monomer at the edge of the surface, becoming a ledge adatom (S4). The dissolution of Ca²⁺ from the kink site involving chemical bond breakage ends here and the next stage is the desorption of the adsorbed Ca²⁺-water complex from the ledge or terrace sites into the solution.

The last transition state (TS4) is so-call "outer-sphere adsorption", beyond which the diffusion process of the dissolved Ca²⁺ ion starts. The desorption free energy barrier is ~29 kJ/mol, which is comparable with previous the study of potassium desorption on orthoclase surfaces (~22 kJ/mol) [39]. Due to the fact that Ca²⁺ at the ledge adatom state (S4) is apt to move around the terrace surface rather than move backwards to the previous states (S1-S3), the bond-breakage stage at the kink site (S1-S4) and the desorption stage from ledge or terrace sites (S4-TS4) should be regarded as two sequential reactions. Therefore, the entire dissolution kinetics is governed by the former stage (S1-S4) with a total free energy barrier of ~63 kJ/mol.

The aforementioned intermediate and transition states with thermodynamic information portray a mechanistic picture of the dissolution process that is currently difficult to capture experimentally. Yet, the energetics of the dissolution process can be compared with the available experimental results for validity. There are some experimentally measured apparent hydration/dissolution activation energies of β -C₂S available from the literature. For example, Thomas *et al.* measured the hydration activation energy of the standard and "reactive" (calcined at lower temperature and with the high surface area) β -C₂S specimens, obtaining ~32 kJ/mol and ~55 kJ/mol respectively. Considering the degree of hydration, Taylor [1] suggests that the apparent activation energy of β -C₂S hydration is ~56 kJ/mol. While these activation energies are fitted with calorimetry-based measurements and do not strictly reflect the single dissolution process, they can still validate our calculated dissolution free energy barriers in view of the order of magnitude.

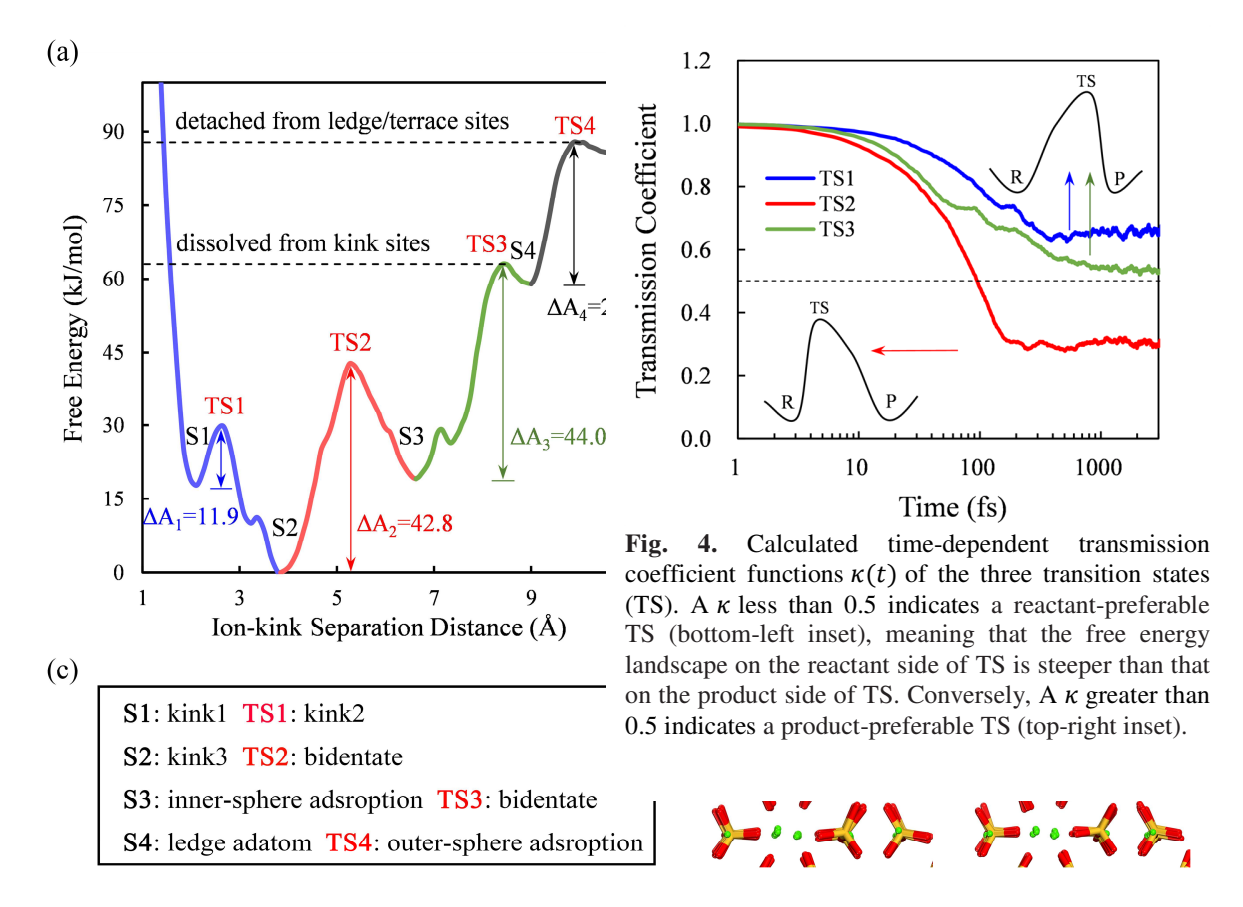


Fig. 3. Free energy profile (a) and configurations of intermediate and transition states (b) of the Ca^{2+} ion dissolution from a kink site on (1 0 0) β- C_2S surface. The free energy profiles of reaction steps are distinguished by different colors and the dashed line shows the energy barriers for the two main dissolution stages. For the configurations of states, some atoms (Ca, H, OH⁻, and H₂O) are hidden to provide clear visualization of the coordination structure of the dissolved Ca^{2+} ion. The black and pink dashed lines depict the chemical bonds (coordination) of the Ca^{2+} ion with the initial kink site and water molecules (H₂O and OH⁻), respectively. The green dashed lines show the chemical bond formation of the Ca^{2+} ion as a ledge adatom. The intermediate and transition states of inset (b) are termed based on the geochemistry (c).

3.2 Kinetics of Ca^{2+} Dissolution: Based on the calculated dissolution free energy profile, the kinetics of Ca^{2+} dissolution can be further calculated. Here, we focus on the bond breakage stage (S1-S4) as the rate-limiting dissolution step. The calculation of kinetic properties requires the measurement of the recrossing ratio when the Ca^{2+} ion reaches a TS, *i.e.*, the probability of reaching the product state. **Fig. 4** shows the time-dependent functions $\kappa(t)$ of the three transition states (TS1, TS2, and TS3) in **Fig. 3**. Performing reactive flux simulations, $\kappa(t)$ is averaged by releasing a large number of statistically independent trajectories at each TS, see **section 2.3**. Since the free energy landscape at the transition state is usually steep, $\kappa(t)$ tends to converge within a few picoseconds. For the Ca^{2+} ion dissolution, $\kappa(t)$ curves level off

after ~1 ps of simulation. However, to obtain a more accurate estimate of κ , we extend the simulation time to 5 ps, and the constant κ is taken by averaging the last 3 ps of $\kappa(t)$ curves.

366367

368

369370

371372

373

374375

The physical meaning of κ is the probability that the system can effectively reach the product state after crossing TS. Therefore, the magnitude of κ reflects, to some extent, the morphological characteristics of the free energy landscape at TS. For a symmetrically distributed free energy landscape at TS, about half of the trajectory leaves TS to reach the product state and the other half recrosses TS to reach the reactant state, which gives a κ of 0.5. A κ less than 0.5 means that less than half of the trajectories starting from TS finally reach the product state, which indicates a reactant-preferable TS (the bottom-left inset of **Fig.** 4). Therefore, the free energy landscape on the left (reactant side) of TS is steeper than that on the right (product side) of TS. Conversely, A κ greater than 0.5 implies a product-preferable TS (the top-right inset of **Fig.** 4). Therefore, TS1 and TS3 have product-preferable TS characteristics, while TS2 is the reactant-preferable TS.

Based on these transmission coefficients (**Fig. 4**) and the free energy profiles (**Fig. 3**), **Table 1** presents the calculated rate and equilibrium constants for each dissolution step and the entire dissolution process. For the three dissolution steps, the rate constants of the forward (k^f) and backward (k^b) reactions are calculated, respectively. Based on the forward and backward rate constants, the equilibrium constant for each dissolution step (K_i) can be calculated[54]:

381
$$S1 \stackrel{k_1^f}{\rightleftharpoons} S2 : K_1 = \frac{k_1^f}{k_1^b} = \frac{[S2]}{[S1]}$$
 (6)

382
$$S_{2} \stackrel{k_{2}^{f}}{\rightleftharpoons} S_{3} : K_{2} = \frac{k_{2}^{f}}{k_{2}^{b}} = \frac{[S_{3}]}{[S_{2}]}$$
 (7)

383
$$S_3 \stackrel{k_3^f}{\rightleftharpoons} S_4 : K_3 = \frac{k_3^f}{k_3^b} = \frac{[S_4]}{[S_3]}$$
 (8)

where [X] represents the activity of specie X. Therefore, the total equilibrium constant of the overall dissolution reaction can be written as:

386
$$K = K_1 K_2 K_3 = \frac{[S4]}{[S1]}$$
 (9)

Since the activity of the solid reactant (kink surface) is unity during the simulation, the total equilibrium constant K is equal to the activity of Ca^{2+} ions, which is $\sim 1.03 \times 10^{-5}$. Available experimental data show that the Ca^{2+} ion activity is $2.44 \times 10^{-5} - 8.75 \times 10^{-5}$ at the dissolution degree of 6% - 11% for β -C₂S [11].

The Ca²⁺ ion activity is observed variable with the dissolution degree and alkalinity. It should also be noted that the calculated free energy profile could have some differences with that in an equilibrium condition where the experimental ion activities are obtained from. Considering the differences of conditions for the experiments and our simulations, the calculated Ca²⁺ ion activity serves only as a qualitative comparison.

390

391

392

393394

395

396

397

398399

400

401 402

403

404

405

406

407

408

409

410

411

412

413

414

415 416

417

418

419 420

421

422

As the thermodynamics and kinetics of Ca²⁺ ions are revealed, one naturally asks what role the [SiO₄] silicate group plays in the dissolution process of β-C₂S. Although this paper mainly discusses the dissolution process of Ca²⁺ ions, we can theoretically discuss the dissolution characteristics of [SiO₄] groups qualitatively. According to eq. (2), at a given temperature, the reaction rate constant is inversely correlated with the free energy barriers of TS and the reduced mass. While the dissolution free energy of the [SiO₄] group is not calculated here, the free energy barriers are supposed to be larger than that of Ca²⁺ ion dissolution since dissolving a [SiO₄] group needs to break much more chemical bonds from the surface. On the other hand, the mass of H₄SiO₄ is much larger than that of Ca. Therefore, the dissolution rate of H₄SiO₄ is supposed to be significantly smaller than that of Ca ions, which implies the dissolution of clinker minerals is non-stoichiometric, i.e., incongruent dissolution. In fact, incongruent dissolution has been widely confirmed in the literature for the cement minerals [14, 76, 77] and olivine minerals [78-80]. For example, for the dissolution process of C₃A [14], after the rapid dissolution of Ca ions, a large amount of $[H_mAlO_4]^{n-}$ remains on the surface to form an aluminum-rich layer, which is charged and can absorb ions from the solution to form hydration products on the surface. Tadros et al. [77] studied the dissolution of C₃S and found that the ratio of Ca²⁺/H₂SiO₄²⁻ in the solution was much greater than the stoichiometric ratio of Ca/Si in C₃S. They also found that the surface of C₃S particles was positively charged because Ca²⁺ ions were adsorbed on the surface. Therefore, we can roughly describe the dissolution process of clinker minerals as follows. When clinker minerals contact water, Ca²⁺ ions in the forefront layer of the solid-liquid interface dissolve rapidly, forming atomic holes on the surface and leaving the hydroxylated [SiO₄] or [AlO₄] groups (HSiO₄³⁻, H₂SiO₄²⁻, H₃SiO₄⁻, etc.) highly uncoordinated on the surface. These surface defects were described as the so-called two-dimensional vacancy islands in the dissolution and nucleation mechanisms proposed by Cabrera et al. [81], which have recently been adopted by Juilland et al. [19] to explain the fast dissolution of clinker minerals at early hydration stage. After massive Ca2+ ions dissolved from the forefront layers, the Ca2+ dissolution slows down until the [SiO₄] or [AlO₄] groups are removed from the surface to make fresh surfaces that expose Ca²⁺ ions to the solution. Juilland et al. [19] regarded this process as "step retreat" that causes the rapid decrease of clinker dissolution, *i.e.*, the start of the induction period.

Table 1 Calculated kinetic properties of Ca²⁺ ion dissolution from (1 0 0) β-C₂S surface at each dissolution stage.

reaction	direction	k^{TST} (s ⁻¹)	κ	k (s ⁻¹)	K_i	K
61 > 62	forward	3.06E+10	0.658	2.02E+10	3.43E+03	
S1 ≠ S2	backward	1.72E+07	0.342	5.88E+06	3.43E+03	
60 / 60	forward	8.88E+04	0.304	2.70E+04	2.000.04	1.03E-05
S2 ≥ S3	backward	1.30E+08	0.696	9.07E+07	2.98E-04	
GQ . G4	forward	3.55E+04	0.545	1.94E+04	1.015.05	
S3 ≠ S4	backward	4.20E+09	0.456	1.91E+09	1.01E-05	

3.3 Surface Effects on the Ca²⁺ Diffusion: Since we have unveiled the thermodynamics and kinetics of a
Ca²⁺ dissolution process from a kink site, here we further discuss the surface effects on the diffusion
process of Ca²⁺ in solution after it departs the surface. We calculated the self-diffusion coefficients of
Ca²⁺ ions near an uncharged kink surface, flat surface, and in the aqueous water at different temperatures
(Table 2). The self-diffusion activation energy is calculated by fitting the Arrhenius equation:

428
$$\ln D = -\frac{E_a}{R} \frac{1}{T} + \ln D_0$$
 (5)

where E_a is the diffusion activation energy, D_0 is the maximal diffusion coefficient at infinite temperature, and R is the universal gas constant. As shown in **Table 2**, the calculated self-diffusion coefficients of Ca^{2+} ions at the room temperature are in the range of $7.28 \times 10^{-10} - 9.32 \times 10^{-10}$ m²/s, which is in agreement with the experimentally measured value of 7.9×10^{-10} m²/s in dilute solutions [82, 83]. The slight difference between the simulation and experiments can be related to the concentration effect (*i.e.*, self-diffusion coefficients decrease with the increase of ion concentration [84]) and finite size effect (*e.g.*, lower dielectric permittivity constant) of the

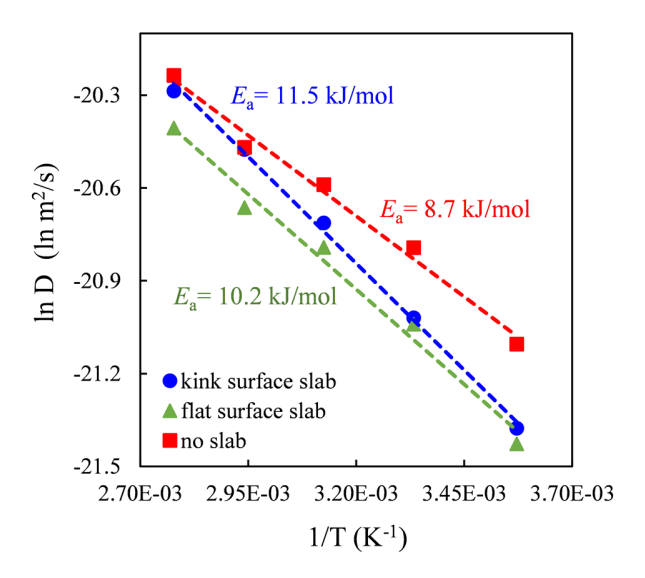


Fig. 5. Diffusion coefficients of Ca²⁺ ions in the solution of the kink surface slab, flat surface slab, and water box at different temperatures. The apparent activation energy is calculated by fitting the Arrhenius equation.

current models that can affect ion correlation forces [85]. According to the finite size correction method proposed by Yeh and Hummer [86], the finite size effect decreases with the increase of the box length. Provided the linear relationship holds valid, the relative errors between the calculated and corrected diffusion coefficients in our case is ~5%, which does not influence the qualitative comparison of the Ca²⁺ diffusion properties in the three diffusion models.

As shown in **Fig. 5**, the surface effects lower the diffusion coefficients of Ca²⁺ especially at low temperatures. It is mainly because the Ca²⁺ ions and water molecules near the surface possess lower mobility than that in the bulk solution due to the interactions with the surface ions. These surface interactions are clearly revealed by the larger diffusion activation energy for the slab models in respect to the no slab model. The low mobility of water molecules near the surface has been experimentally characterized via proton field-cycling relaxometry [87] and neutron elastic backscattering measurements [88]. Masoumi *et al.* [85, 89] showed that the interfacial water (~ 2-3 layers above the surface) is structured compared with the bulk water. Kerisit *et al.* [38, 39] have also shown the presence of a strong surface-water interaction on orthoclase and forsterite minerals. As the temperature increases, the interactions between Ca²⁺ ions and the surface ions are rapidly weakened since the thermal vibration of ions is strikingly enhanced. Thus, the surface effects are receding and the diffusion coefficients of the slab models are getting close to that of the no slab model. The diffusion coefficients of the flat surface slab are lower and less sensitive to temperature compared with the kink surface slab mainly because the flat

surface is more regulated to produce stronger interactions with the Ca²⁺ ions and water molecules in the solution.

Table 2 Calculated Ca^{2+} diffusion coefficients (*D*) in the solution of the kink surface slab, flat surface slab, and water box at scaling temperatures. The diffusion activation energy (E_a) and the maximal diffusion coefficients at infinite temperature (D_0) are fitted based on the Arrhenius law.

T(K)	kink surface slab		flat surface slab			water box (no slab)			
	$D (\text{m}^2/\text{s})$	E _a (kJ/mol)	$D_0 ({\rm m^2/s})$	D (m ² /s)	E _a (kJ/mol)	$D_0 ({\rm m^2/s})$	D (m ² /s)	E _a (kJ/mol)	$D_0 ({\rm m^2/s})$
360	1.55E-09			1.37E-09			1.63E-09		
340	1.28E-09			1.06E-09			1.29E-09		
320	1.01E-09	11.48	7.35E-08	9.34E-10	10.21	4.15E-08	1.14E-09	8.679	2.91E-08
300	7.43E-10			7.28E-10			9.32E-10		
280	5.21E-10			4.95E-10			6.83E-10		

5. Conclusions and Outlook

This paper presents an atomistic simulation framework to study the thermodynamics and kinetics of β -C₂S dissolution. Combining metadynamics and umbrella sampling methods, we unravel the mechanistic picture of Ca²⁺ dissolution that is comprised of two sequential stages: breaking restraints from the kink sites to form a ledge adatom and detaching from the ledge/terrace adatom sites into the solution. At the first stage, the chemical bonds between the dissolving Ca²⁺ ion and the adjacent silicate monomers at the initial kink site are progressively broken to form bidentate and inner-sphere adsorption. As the last chemical bond with the kink site is broken, the Ca²⁺ ion forms a new chemical bond with the silicate monomer at the edge of the surface, becoming a ledge adatom. For the second stage, the adsorbed Ca²⁺-water complex detaches from the ledge/terrace adatom sites to form outer-sphere adsorption, where the diffusion process starts. The first and second stages feature free energy barriers of ~63 kJ/mol and ~29 kJ/mol respectively. The entire Ca²⁺ dissolution kinetics is therefore governed by the first stage. Using the reactive flux method, the rate and equilibrium constants for each reaction step are calculated. Aggregating these results yields the Ca²⁺ ion activity of ~1.03×10⁻⁵. The diffusion calculations indicate that the surface effects significantly lower the diffusion coefficients of Ca²⁺ ions in the solution and the effects are mitigated at high temperatures.

Through this work, we present a detailed mechanistic picture and energetics of the β -C₂S dissolution process at the nanoscale. The methodology proposed in this work can be extended to investigate other surface defects (*e.g.*, dislocations, steps, adatoms, *etc.*), cleavages, and natural and synthetic minerals.

- While we compare our results with available experimental data, we emphasize that there is a clear scale
- 490 separation between our simulations and mesoscale dissolution processes such as etch pit formation and
- step retreat. This calls for the development of multiscale models that hierarchically inform each other by
- 492 passing thermodynamic and kinetic data. An ideal framework would be to combine our approach with the
- recently developed kinetic Monte Carlo methods[21] to obtain a holistic picture of the dissolution process
- of cement minerals from the nano- to meso-scale. Such a transferable multiscale model can be ultimately
- leveraged to pave the path for *in silico* design and optimization of sustainable clinker formulations.

496 **Author Information**

497 Corresponding Author:

500

504

516

- * E-mail: fzhwang@whut.edu.cn (Fazhou Wang)
- * E-mail: mjaq@uci.edu (Mohammad Javad Abdolhosseini Qomi)

CRediT authorship contribution statement:

- 501 Y. T.: Conceptualization, Methodology, Software, Visualization, Writing Original Draft. S. Z.:
- Methodology, Software. F. W.: Supervision, Resources. M. J. A. Q.: Conceptualization, Writing Review
- 503 & Editing, Supervision, Resources.

Declaration of competing interest:

- The authors declare that they have no known competing financial interests or personal relationships that
- 506 could have appeared to influence the work reported in this paper.

507 Acknowledgements:

- 508 The authors would like to sincerely thank Dr. Mehdi Shishehbor and Mr. Ali Morshedi for the fruitful
- discussions and assistance in programming. Y.T. and F.W. contributions were supported by The National
- 510 Science Fund for Distinguished Young Scholars (grant number 51925205); China Scholarship Council
- 511 (201906950033). M.J.A.Q. contributions were supported by the U.S. Department of Energy (DOE),
- 512 Office of Science, Office of Basic Energy Sciences (BES), Chemical Sciences, Geosciences, and
- 513 Biosciences Division through its Geosciences program at the University of California Irvine through an
- Early Career award (DE-SC0022301). S.Z. contributions were supported by the U.S. National Science
- Foundation grant CMMI-2103125

References:

- 517 [1] H.F.W. Taylor, Cement Chemistry, 2nd edition, Thomas Telford, London, 1997.
- 518 [2] W. Kurdowski, S. Duszak, B. Trybalska, Belite produced by means of low-temperature synthesis,
- 519 Cement and Concrete Research, 27 (1997) 51-62.

- 520 [3] A. Cuesta, A. Ayuela, M.A.G. Aranda, Belite cements and their activation, Cement and Concrete
- 521 Research, 140 (2021) 106319.
- 522 [4] H.-M. Ludwig, W. Zhang, Research review of cement clinker chemistry, Cement and Concrete
- 523 Research, 78 (2015) 24-37.
- 524 [5] T. Staněk, P. Sulovský, Active low-energy belite cement, Cement and Concrete Research, 68 (2015)
- 525 203-210.
- 526 [6] S. Rahimi-Aghdam, Z.P. Bažant, M.J. Abdolhosseini Qomi, Cement hydration from hours to centuries
- 527 controlled by diffusion through barrier shells of C-S-H, Journal of the Mechanics and Physics of Solids, 99
- 528 (2017) 211-224.
- 529 [7] K. Scrivener, A. Ouzia, P. Juilland, A. Kunhi Mohamed, Advances in understanding cement hydration
- mechanisms, Cement and Concrete Research, 124 (2019) 105823.
- 531 [8] S. Ye, P. Feng, Y. Liu, J. Liu, J.W. Bullard, In situ nano-scale observation of C₃A dissolution in water,
- 532 Cement and Concrete Research, 132 (2020) 106044.
- 533 [9] J.J. Thomas, S. Ghazizadeh, E. Masoero, Kinetic mechanisms and activation energies for hydration of
- standard and highly reactive forms of β-dicalcium silicate (C₂S), Cement and Concrete Research, 100
- 535 (2017) 322-328.
- 536 [10] J.J. Thomas, The instantaneous apparent activation energy of cement hydration measured using a
- 537 novel calorimetry-based method, Journal of the American Ceramic Society, 95 (2012) 3291-3296.
- [11] L. Nicoleau, A. Nonat, D. Perrey, The di- and tricalcium silicate dissolutions, Cement and Concrete
- 539 Research, 47 (2013) 14-30.
- 540 [12] A.S. Brand, J.M. Gorham, J.W. Bullard, Dissolution rate spectra of β-dicalcium silicate in water of
- varying activity, Cement and Concrete Research, 118 (2019) 69-83.
- 542 [13] A.S. Brand, J.W. Bullard, Dissolution kinetics of cubic tricalcium aluminate measured by digital
- holographic microscopy, Langmuir, 33 (2017) 9645-9656.
- 544 [14] R.J. Myers, G. Geng, J. Li, E.D. Rodriguez, J. Ha, P. Kidkhunthod, G. Sposito, L.N. Lammers, A.P.
- 545 Kirchheim, P.J. Monteiro, Role of adsorption phenomena in cubic tricalcium aluminate dissolution,
- 546 Langmuir, 33 (2017) 45-55.
- [15] K. Miyata, J. Tracey, K. Miyazawa, V. Haapasilta, P. Spijker, Y. Kawagoe, A.S. Foster, K. Tsukamoto, T.
- 548 Fukuma, Dissolution processes at step edges of calcite in water investigated by high-speed frequency
- modulation atomic force microscopy and simulation, Nano letters, 17 (2017) 4083-4089.
- [16] I. Bibi, R. Arvidson, C. Fischer, A. Lüttge, Temporal evolution of calcite surface dissolution kinetics,
- 551 Minerals, 8 (2018) 256.
- 552 [17] J.J. Thomas, J.J. Biernacki, J.W. Bullard, S. Bishnoi, J.S. Dolado, G.W. Scherer, A. Luttge, Modeling
- and simulation of cement hydration kinetics and microstructure development, Cement and Concrete
- 554 Research, 41 (2011) 1257-1278.
- 555 [18] P.M. Dove, N. Han, J.J. De Yoreo, Mechanisms of classical crystal growth theory explain quartz and
- silicate dissolution behavior, Proceedings of the National Academy of Sciences, 102 (2005) 15357-15362.
- 557 [19] P. Juilland, E. Gallucci, R. Flatt, K. Scrivener, Dissolution theory applied to the induction period in
- alite hydration, Cement and Concrete Research, 40 (2010) 831-844.
- 559 [20] J.W. Bullard, A determination of hydration mechanisms for tricalcium silicate using a kinetic cellular
- automaton model, Journal of the American Ceramic Society, 91 (2008) 2088-2097.
- 561 [21] P. Martin, H. Manzano, J.S. Dolado, Mechanisms and dynamics of mineral dissolution: A new kinetic
- Monte Carlo model, Advanced Theory and Simulations, 2 (2019) 1900114.
- 563 [22] K. Coopamootoo, E. Masoero, Simulations of crystal dissolution using interacting particles:
- 564 Prediction of stress evolution and rates at defects and application to tricalcium silicate, The Journal of
- 565 Physical Chemistry C, 124 (2020) 19603-19615.

- 566 [23] J. Chen, P. Martin, Z. Xu, H. Manzano, J.S. Dolado, G. Ye, A dissolution model of alite coupling
- surface topography and ions transport under different hydrodynamics conditions at microscale, Cement
- 568 and Concrete Research, 142 (2021) 106377.
- 569 [24] Y. Tao, W. Zhang, N. Li, F. Wang, S. Hu, Atomic occupancy mechanism in brownmillerite Ca₂FeAlO₅
- from a thermodynamic perspective, Journal of the American Ceramic Society, 103 (2019) 635-644.
- 571 [25] Y. Tao, W. Zhang, N. Li, F. Wang, S. Hu, Predicting hydration reactivity of Cu-doped clinker crystals
- 572 by capturing electronic structure modification, ACS Sustainable Chemistry & Engineering, 7 (2019) 6412-
- 573 6421.
- 574 [26] E. Durgun, H. Manzano, P.V. Kumar, J.C. Grossman, The characterization, stability, and reactivity of
- 575 synthetic calcium silicate surfaces from first principles, The Journal of Physical Chemistry C, 118 (2014)
- 576 15214-15219
- 577 [27] H. Manzano, E. Durgun, I. Lopez-Arbeloa, J.C. Grossman, Insight on tricalcium silicate hydration and
- 578 dissolution mechanism from molecular simulations, ACS applied materials & interfaces, 7 (2015) 14726-
- 579 14733.
- 580 [28] E. Durgun, H. Manzano, R.J.M. Pellenq, J.C. Grossman, Understanding and controlling the reactivity
- of the calcium silicate phases from first principles, Chem. Mater., 24 (2012) 1262-1267.
- 582 [29] G. Bussi, A. Laio, Using metadynamics to explore complex free-energy landscapes, Nature Reviews
- 583 Physics, 2 (2020) 200-212.
- 584 [30] A. Laio, M. Parrinello, Escaping free-energy minima, Proceedings of the National Academy of
- 585 Sciences, 99 (2002) 12562.
- 586 [31] G. Torrie, J. Valleau, Monte Carlo study of a phase separating liquid mixture by umbrella sampling,
- 587 The Journal of Chemical Physics, 66 (1977) 1402-1408.
- 588 [32] G.M. Torrie, J.P. Valleau, Monte Carlo free energy estimates using non-Boltzmann sampling:
- Application to the sub-critical Lennard-Jones fluid, Chemical Physics Letters, 28 (1974) 578-581.
- 590 [33] E. Darve, A. Pohorille, Calculating free energies using average force, The Journal of Chemical
- 591 Physics, 115 (2001) 9169-9183.
- 592 [34] R.W. Zwanzig, High temperature equation of state by a perturbation method. I. Nonpolar gases,
- 593 The Journal of Chemical Physics, 22 (1954) 1420-1426.
- 594 [35] R.K. Mishra, A.K. Mohamed, D. Geissbühler, H. Manzano, T. Jamil, R. Shahsavari, A.G. Kalinichev, S.
- 595 Galmarini, L. Tao, H. Heinz, R. Pellenq, A.C.T. van Duin, S.C. Parker, R.J. Flatt, P. Bowen, *cemff*: A force
- 596 field database for cementitious materials including validations, applications and opportunities, Cement
- 597 and Concrete Research, 102 (2017) 68-89.
- 598 [36] H. Manzano, S. Moeini, F. Marinelli, A.C. van Duin, F.J. Ulm, R.J. Pelleng, Confined water dissociation
- 599 in microporous defective silicates: Mechanism, dipole distribution, and impact on substrate properties,
- Journal of the American Chemical Society, 134 (2012) 2208-2215.
- 601 [37] R.T. Cygan, J.-J. Liang, A.G. Kalinichev, Molecular models of hydroxide, oxyhydroxide, and clay
- phases and the development of a general force field, The Journal of Physical Chemistry B, 108 (2004)
- 603 1255-1266.
- 604 [38] S. Kerisit, J.H. Weare, A.R. Felmy, Structure and dynamics of forsterite–scCO₂/H₂O interfaces as a
- function of water content, Geochimica et Cosmochimica Acta, 84 (2012) 137-151.
- 606 [39] S. Kerisit, C. Liu, E.S. Ilton, Molecular dynamics simulations of the orthoclase (001)- and (010)-water
- interfaces, Geochimica et Cosmochimica Acta, 72 (2008) 1481-1497.
- 608 [40] S. Kerisit, S.C. Parker, Free energy of adsorption of water and metal ions on the {1014} calcite
- surface, Journal of the American Chemical Society, 126 (2004) 10152-10161.
- 610 [41] P. Raiteri, R. Demichelis, J.D. Gale, Thermodynamically consistent force field for molecular dynamics
- simulations of alkaline-earth carbonates and their aqueous speciation, The Journal of Physical Chemistry
- 612 C, 119 (2015) 24447-24458.

- 613 [42] Y. Tao, W. Zhang, D. Shang, Z. Xia, N. Li, W.-Y. Ching, F. Wang, S. Hu, Comprehending the occupying
- preference of manganese substitution in crystalline cement clinker phases: A theoretical study, Cement
- 615 and Concrete Research, 109 (2018) 19-29.
- 616 [43] C. Dharmawardhana, M. Bakare, A. Misra, W.-Y. Ching, Nature of interatomic bonding in controlling
- 617 the mechanical properties of calcium silicate hydrates, Journal of the American Ceramic Society, 99
- 618 (2016) 2120-2130.
- 619 [44] H. Manzano, J.S. Dolado, A. Ayuela, Elastic properties of the main species present in Portland
- 620 cement pastes, Acta Materialia, 57 (2009) 1666-1674.
- 621 [45] K.H. Jost, B. Ziemer, R. Seydel, Redetermination of the structure of β-dicalcium silicate, Acta
- 622 Crystallogr. B, 33 (1977) 1696–1700.
- 623 [46] M.J. Abdolhosseini Qomi, F.-J. Ulm, R.J.M. Pellenq, Physical origins of thermal properties of cement
- 624 paste, Physical Review Applied, 3 (2015) 064010.
- 625 [47] J.P. Perdew, K. Burke, M. Ernzerhof, Generalized gradient approximation made simple, Phys. Rev.
- 626 Lett., 77 (1996).
- [48] B. PE, Projector augmented-wave method, Physical Review B, 50 (1994) 17953-17979.
- 628 [49] S. Grimme, J. Antony, S. Ehrlich, H. Krieg, A consistent and accurate ab initio parametrization of
- density functional dispersion correction (DFT-D) for the 94 elements H-Pu, The Journal of Chemical
- 630 Physics, 132 (2010) 154104.
- [50] J.D. Gale, GULP: A computer program for the symmetry-adapted simulation of solids, Journal of the
- 632 Chemical Society, Faraday Transactions, 93 (1997) 629-637.
- 633 [51] I.N. Stranski, Zur theorie des kristallwachstums, Zeitschrift für physikalische Chemie, 136 (1928)
- 634 259-278.
- [52] W. Kossel, Extenoling the law of bravais, Nach. Ges. Wiss. Gottingen, 143 (1927) 25.
- [53] J.N. Bracco, A.G. Stack, C.I. Steefel, Upscaling calcite growth rates from the mesoscale to the
- macroscale, Environmental science & technology, 47 (2013) 7555-7562.
- 638 [54] A.G. Stack, P. Raiteri, J.D. Gale, Accurate rates of the complex mechanisms for growth and
- dissolution of minerals using a combination of rare-event theories, Journal of the American Chemical
- 640 Society, 134 (2012) 11-14.
- [55] K. Mori, R. Kiyanagi, M. Yonemura, K. Iwase, T. Sato, K. Itoh, M. Sugiyama, T. Kamiyama, T.
- 642 Fukunaga, Charge states of Ca atoms in β-dicalcium silicate, Journal of Solid State Chemistry, 179 (2006)
- 643 3286-3294.
- [56] Y. Tao, N. Li, W. Zhang, F. Wang, S. Hu, Understanding the zinc incorporation into silicate clinker
- during waste co-disposal of cement kiln: A density functional theory study, Journal of Cleaner
- 646 Production, 232 (2019) 329-336.
- 647 [57] H. Yan, C. Park, G. Ahn, S. Hong, D.T. Keane, C. Kenney-Benson, P. Chow, Y. Xiao, G. Shen,
- Termination and hydration of forsteritic olivine (0 1 0) surface, Geochimica Et Cosmochimica Acta, 145
- 649 (2014) 268-280.
- 650 [58] T. Liu, S.S. Gautam, L.L. Daemen, A.I. Kolesnikov, L.M. Anovitz, M. Hartl, D.R. Cole, Vibrational
- behavior of water adsorbed on forsterite (Mg₂SiO₄) surfaces, ACS Earth and Space Chemistry, 4 (2020)
- 652 1050-1063.
- 653 [59] N.H. de Leeuw, S.C. Parker, C.R.A. Catlow, G.D. Price, Modelling the effect of water on the surface
- 654 structure and stability of forsterite, Physics and Chemistry of Minerals, 27 (2000) 332-341.
- 655 [60] Q. Wang, H. Manzano, Y. Guo, I. Lopez-Arbeloa, X. Shen, Hydration mechanism of reactive and
- 656 passive dicalcium silicate polymorphs from molecular simulations, The Journal of Physical Chemistry C,
- 657 119 (2015) 19869-19875.
- 658 [61] S. Plimpton, Fast parallel algorithms for short-range molecular dynamics, Journal of computational
- 659 physics, 117 (1995) 1-19.

- 660 [62] A. Barducci, M. Bonomi, M. Parrinello, Metadynamics, Wiley Interdisciplinary Reviews:
- 661 Computational Molecular Science, 1 (2011) 826-843.
- 662 [63] J. Kästner, Umbrella sampling, Wiley Interdisciplinary Reviews: Computational Molecular Science, 1
- 663 (2011) 932-942.
- 664 [64] G. Henkelman, H. Jónsson, Improved tangent estimate in the nudged elastic band method for
- 665 finding minimum energy paths and saddle points, The Journal of Chemical Physics, 113 (2000) 9978-
- 666 9985.
- [65] M.N. Joswiak, M.F. Doherty, B. Peters, Ion dissolution mechanism and kinetics at kink sites on NaCl
- 668 surfaces, Proc Natl Acad Sci U S A, 115 (2018) 656-661.
- 669 [66] Z. Bjelobrk, D. Mendels, T. Karmakar, M. Parrinello, M. Mazzotti, Solubility prediction of organic
- 670 molecules with molecular dynamics simulations, Crystal Growth & Design, 21 (2021) 5198-5205.
- [67] Z. Shen, S.N. Kerisit, A.G. Stack, K.M. Rosso, Free-energy landscape of the dissolution of gibbsite at
- 672 high pH, The journal of physical chemistry letters, 9 (2018) 1809-1814.
- [68] L. Helm, A.E. Merbach, Water exchange on metal ions: experiments and simulations, Coordination
- 674 Chemistry Reviews, 187 (1999) 151-181.
- 675 [69] W.H. Casey, H.R. Westrich, Control of dissolution rates of orthosilicate minerals by divalent metal-
- 676 oxygen bonds, Nature, 355 (1992) 157-159.
- 677 [70] M. De La Pierre, P. Raiteri, J.D. Gale, Structure and dynamics of water at step edges on the calcite
- 678 {1014} surface, Crystal Growth & Design, 16 (2016) 5907-5914.
- 679 [71] M. Bonomi, D. Branduardi, G. Bussi, C. Camilloni, D. Provasi, P. Raiteri, D. Donadio, F. Marinelli, F.
- 680 Pietrucci, R.A. Broglia, M. Parrinello, PLUMED: A portable plugin for free-energy calculations with
- 681 molecular dynamics, Computer Physics Communications, 180 (2009) 1961-1972.
- 682 [72] A. Barducci, G. Bussi, M. Parrinello, Well-tempered metadynamics: A smoothly converging and
- tunable free-energy method, Physical review letters, 100 (2008) 020603.
- 684 [73] B.J. Berne, G. Ciccotti, D.F. Coker, Classical and quantum dynamics in condensed phase simulations:
- Proceedings of the International School of Physics, World Scientific1998.
- 686 [74] D. Chandler, Statistical mechanics of isomerization dynamics in liquids and the transition state
- approximation, The Journal of Chemical Physics, 68 (1978) 2959-2970.
- 688 [75] M.J.A. Qomi, M. Bauchy, F.-J. Ulm, R.J.-M. Pelleng, Anomalous composition-dependent dynamics of
- 689 nanoconfined water in the interlayer of disordered calcium-silicates, The Journal of Chemical Physics,
- 690 140 (2014) 054515.
- 691 [76] G. Rim, N. Roy, D. Zhao, S. Kawashima, P. Stallworth, S.G. Greenbaum, A.-H.A. Park, CO₂ utilization
- 692 in built environment via the P_{CO2} swing carbonation of alkaline solid wastes with different mineralogy,
- 693 Faraday Discussions, (2021).
- 694 [77] M.E. Tadros, J.A.N. Skalny, R.S. Kalyoncu, Early hydration of tricalcium silicate, Journal of the
- 695 American Ceramic Society, 59 (1976) 344-347.
- 696 [78] E.H. Oelkers, J. Declercq, G.D. Saldi, S.R. Gislason, J. Schott, Olivine dissolution rates: A critical
- 697 review, Chemical Geology, 500 (2018) 1-19.
- 698 [79] F.K. Crundwell, The mechanism of dissolution of forsterite, olivine and minerals of the orthosilicate
- 699 group, Hydrometallurgy, 150 (2014) 68-82.
- 700 [80] J.D. Rimstidt, S.L. Brantley, A.A. Olsen, Systematic review of forsterite dissolution rate data,
- 701 Geochimica et Cosmochimica Acta, 99 (2012) 159-178.
- 702 [81] N. Cabrera, M. Levine, XLV. On the dislocation theory of evaporation of crystals, Philosophical
- 703 Magazine, 1 (1956) 450-458.
- 704 [82] C. Pichler, A. Saxer, R. Lackner, Differential-scheme based dissolution/diffusion model for calcium
- 705 leaching in cement-based materials accounting for mix design and binder composition, Cement and
- 706 Concrete Research, 42 (2012) 686-699.

- 707 [83] Y.A. Le Gouellec, M. Elimelech, Control of calcium sulfate (gypsum) scale in nanofiltration of saline 708 agricultural drainage water, Environmental Engineering Science, 19 (2002) 387-397.
- 709 [84] J.H. Wang, Tracer-diffusion in liquids. IV. Self-diffusion of calcium ion and chloride ion in aqueous
- 710 calcium chloride solutions1, Journal of the American Chemical Society, 75 (1953) 1769-1770.
- 711 [85] S. Masoumi, S. Zare, H. Valipour, M.J. Abdolhosseini Qomi, Effective interactions between calcium-
- 712 silicate-hydrate nanolayers, The Journal of Physical Chemistry C, 123 (2019) 4755-4766.
- 713 [86] I.-C. Yeh, G. Hummer, System-size dependence of diffusion coefficients and viscosities from
- 714 molecular dynamics simulations with periodic boundary conditions, The Journal of Physical Chemistry B,
- 715 108 (2004) 15873-15879.
- 716 [87] J.-P. Korb, P. McDonald, L. Monteilhet, A. Kalinichev, R. Kirkpatrick, Comparison of proton field-
- 717 cycling relaxometry and molecular dynamics simulations for proton-water surface dynamics in cement-
- 718 based materials, Cement and Concrete Research, 37 (2007) 348-350.
- 719 [88] E. Fratini, A. Faraone, F. Ridi, S.-H. Chen, P. Baglioni, Hydration water dynamics in tricalcium silicate
- 720 pastes by time-resolved incoherent elastic neutron scattering, The Journal of Physical Chemistry C, 117
- 721 (2013) 7358-7364.
- [89] S. Masoumi, H. Valipour, M.J. Abdolhosseini Qomi, Intermolecular forces between nanolayers of 722
- 723 crystalline calcium-silicate-hydrates in aqueous medium, The Journal of Physical Chemistry C, 121 (2017)
- 724 5565-5572.

725